The impact threshold of the aerosol radiative forcing on the boundary layer structure in the pollution region

Dandan Zhao[†1,2], Jinyuan Xin[*†1,2,3], Chongshui Gong[4], Jiannong Quan[5], Yuesi Wang[1,2], Guiqian Tang[1], Yongxiang Ma[1], Lindong Dai[1], Xiaoyan Wu[1], Guangjing Liu[1], Yongjing Ma[1]

1. State Key Laboratory of Atmospheric Boundary Layer Physics and Atmospheric Chemistry (LAPC), Institute of Atmospheric Physics, Chinese Academy of Sciences, Beijing 100029, China

2. University of Chinese Academy of Sciences, Beijing 100049, China

3. Collaborative Innovation Center on Forecast and Evaluation of Meteorological Disasters, Nanjing University of Information Science and Technology, Nanjing, 210044, China

4. Institute of Arid Meteorology, China Meteorological Administration, Lanzhou 730020, China

5. Institute of Urban Meteorology, Chinese Meteorological Administration, Beijing, China

(†) These authors contributed equally to this study.

(*) Correspondence to: Jinyuan Xin (xjy@mail.iap.ac.cn).

Abstract: Recently, there has been increasing interests in the relation between particulate matter (PM) pollution and atmospheric boundary layer (ABL) structure. This study aimed to qualitatively assess the interaction between PM and ABL structure in essence and further quantitatively estimate aerosol radiative forcing (ARF) effects on the ABL structure. Multi-period comparative analysis indicated that the key to determining whether the haze outbreak or dissipation occurs is whether the ABL structure satisfies the relevant conditions. However, the ABL structure change was in turn highly related to the PM level and ARF. |SFC-ATM| (SFC and ATM are the ARFs at the surface and interior of the atmospheric column, respectively) is the absolute difference between ground and atmosphere layer ARFs, and the |SFC-ATM| change is linearly related to the PM concentrations. However, the influence of ARF on the boundary layer structure is nonlinear. With increasing |SFC-ATM|, the TKE level exponentially decreased, which was notable in the lower layers/ABL but disappeared at high altitudes/above the ABL. Moreover, the ARF effects threshold on the ABL structure was determined for the first time, namely, once |SFC-ATM| exceeded ~ 55 W m^{-2}, the ABL structure tends to quickly stabilize and thereafter change little with increasing ARF. The threshold of the ARF effects on the boundary layer structure could provide useful information for relevant atmospheric environment improvement measures and policies, such as formulating phased air pollution control objectives.

1. Introduction

Most urban agglomerations in China, such as the North China Plain (NCP), have suffered from poor air quality due to rapid increase in anthropogenic emissions. Beijing, as the capital city of China and the principal city in the NCP area, has frequently experienced severe and persistent haze events (Li et al., 2020; Wang et al., 2018; Xu et al., 2019; Zhong et al., 2018). Previous studies have found that the occurrence of PM pollution events in Beijing is not only inseparable from the serious primary emissions and fast formation of secondary aerosols (An et al., 2019; Guo et al., 2014; Li et al., 2017; Wang et al., 2014; Zheng et al., 2015; Wang et al., 2012), but also largely affected by the ABL structure, which controls the diffusion, transmission, and accumulation of pollutants (Han et al., 2009; Kotthaus and Grimmond, 2018; Zheng et al., 2017). For instance, the PM concentration has a strong relationship with the ABL height (ABLH) that determines the volume available for pollutant dispersion (Haman et al., 2014; Schaefer et al., 2009; Su et al., 2018; Tang et al., 2016). In most instances, heavy air pollution episodes occurred with persistent temperature inversions (Xu et al., 2019; Zhong et al., 2017). Weak/calm winds are essential in the long-term increase in air pollutants (Niu et al., 2010; Yang et al., 2016). Additionally, severe air pollution is ever reported positively related to high atmospheric humidity, one of the manifestations of stagnant ABL conditions (Tie et al., 2017; Petäjä et al., 2016). Moreover, the feedback mechanism between the boundary layer structure and aerosol loading during severe pollution events contributing to the outbreak of haze pollution has been presented in previous studies (Huang et al., 2018; Liu et al., 2018;

Petäjä et al., 2016; Zhong et al., 2018b; Zhong et al., 2019; Zhao et al., 2019).

However, this topic has yet to be fully understood. More work is needed to systematically study the interaction between ABL structure and PM pollution. Since the surface directly influences the ABL, it is the only atmosphere layer characterized by turbulent activities, while higher atmosphere layers are weakly turbulent because of the strongly stable stratification (Munro, 2005). The ABL acts as a notable turbulence buffer coupling the surface with the free atmosphere, and PM and gas pollutants mainly suspended in the ABL are convectively spread throughout it. The change of boundary layer structure determining the accumulation and diffusion of pollutants in it could be largely linked to the difference of turbulent activity (Garratt et al., 1992). Moreover, the change in solar radiation reaching the ground drives the diurnal ABL evolution (Andrews, 2000). While the diurnal evolution of the atmospheric thermodynamic status could be greatly affected considering a strong aerosol direct radiation effect, namely strongly scattering radiation and absorbing radiation (Dickerson et al., 1997; Liu et al., 2018; Huang et al., 2018; Stone et al., 2008; Zhong et al., 2018a). As previous studies have reported that aerosol absorption and scattering effects during severe air pollution notably enhance atmospheric stability and suppress the boundary layer development (Barbaro et al., 2014; Ding et al., 2016; Wilcox et al., 2016; Yu et al., 2002). Considering the aerosol radiative forcing (ARF) is a critical parameter to quantify the aerosol direct radiation effect (Gong et al., 2014; Li et al., 2018). The influence degree of ARF on the boundary layer structure is still unclear, and thus quantitatively determining the effects of ARF

on the ABL structure is urgently needed.

In this study, we systematically analyzed the way the ABL interacts with PM pollution via contrastive analysis of multiple haze episodes, based on not only specific meteorological factors but also turbulent activity profiles and atmospheric stability indicators. Meanwhile, taking the turbulent kinetic energy (TKE) and ARF as important parameters, we further investigated the influence degree of the aerosol direct radiation effect on the boundary layer structure. Besides, this paper analyzed the interaction between the ABL structure and air pollution using high-resolution and real-observation datasets, such as temperature and humidity profiles of microwave radiometers, horizontal and vertical wind vector profiles of Doppler wind lidar, ABLH, and aerosol backscattering coefficient profiles of ceilometers. Wind profile lidar and microwave radiometers have the advantage of providing direct and continuous observations of the boundary layer over long periods and can characterize the ABL structure up to 2-3 km (Pichugina et al., 2019; Zhao et al., 2019), compensating for the deficiencies of previous research.

2. Data and methods

Figure S1 shows the observation site of the Tower Branch of the Institute of Atmospheric Physics (IAP), Chinese Academy of Sciences (39°58'N, 116°22'E; altitude: 58 m) in Beijing and the sampling instruments in this study. The IAP site is a typical urban Beijing site, and all the sampling instruments are placed at the same location, and simultaneous monitoring is conducted. We conducted a two-month measurement campaign of the PM concentration and aerosol optical depth (AOD) and

obtained vertical profiles of atmospheric parameters such as temperature, humidity, wind vectors, atmospheric stability, and turbulent activity to better understand how the boundary layer structure responds to the aerosol direct radiation effect.

The algorithm of SBDART (Santa Barbara DISORT Atmospheric Radiative Transfer) (Levy et al., 2007) is the core model to calculate the aerosol radiative forcing parameters. More information on the input parameters of SBDART were presented in Table S2. A standard mid-latitude atmosphere is used in SBDART in Beijing. AOD and Ångström Exponent (AE) at 550 nm were obtained from a sun-photometer. Multiple sets of Single Scattering Albedo (SSA) and backscattering coefficient were calculated based on MIE theory, and surface albedo & path radiation were read from MODIS (MOD04), which is used to calculate radiative forcing at the top of atmosphere (TOA). The TOA results were combined with MODIS observations, and the result which has the lowest deviation are defined as the actual parameters of aerosols, and this set of parameters would be used to calculate the radiative forcing at the surface, top, and interior of the atmospheric column (Gong et al., 2014; Lee et al, 2018; Xin et al., 2016). Hourly radiative forcing parameters, including the ARF at the top, surface (SFC), and interior of the atmospheric column (ATM) at an observation site in Beijing can be calculated based on this algorithm. More detailed descriptions are provided in our previous work (Gong et al., 2014; Lee et al, 2018; Xin et al., 2016).

Air temperature and relative and absolute humidity profiles were retrieved with a microwave radiometer (after this referred to as MWR) (RPG-HATPRO-G5 0030109,

Germany). The MWR produces profiles with a resolution ranging from 10-30 m up to 0.5 km, profiles with a resolution ranging from 40-70 m between 0.5 and 2.5 km, and profiles with a resolution ranging from 100-200 m from 2 to 10 km at a temporal resolution of 1 s. More detailed information on the RPG-HATPRO-type instrument can be found at http://www.radiometer-physics.de (last access: 4 June 2020).

Vertical wind speed and horizontal wind vector profiles were obtained by a 3D Doppler wind lidar (Windcube 100s, Leosphere, France). The wind measurement results have a spatial resolution ranging from 1-20 m up to 0.3 km and a spatial resolution of 25 m from 0.3 to 3 km, at a temporal resolution of 5 s. More instrument details can be found at www.leosphere.com (last access: 4 June 2020).

A ceilometer (CL51, Vaisala, Finland) was adopted to acquire atmospheric backscattering coefficient (BSC) profiles. The CL51 ceilometer digitally receives the return backscattering signal from 0 to 100 μs and provides BSC profiles with a spatial resolution of 10 m from the ground to a height of 15 km. The ABLH was further identified by the sharp change in the BSC profile's negative gradient (Münkel et al., 2007), and detailed information is reported in previous studies (Tang et al., 2015, 2016; Zhu et al., 2018).

A CIMEL sun-photometer (CE318, France), a multichannel, automatic sun-and-sky scanning radiometer (Gregory, 2011), was used to observe the AOD, and the AOD at 500 nm is adopted in this paper. The real-time hourly mean ground levels of $PM_{2.5}$ (particulate matter with aerodynamic diameter less than or equal to 2.5 μm) and PM_{10} (particulate matter with aerodynamic diameter less than or equal to 10 μm) were

130 downloaded from the China National Environmental Monitoring Center (CNEMC)
131 (available at http://106.37.208.233:20035/, last access: 4 June 2020).
132 More atmospheric parameters regarding the boundary layer structure used in this
133 study are introduced in S1.
134 **3. Results and discussion**
135 **3.1. General haze episodes over Beijing in winter**
136 It is well known that severe air pollution episodes frequently occur in Beijing
137 during winter (Jin-Xiang, 2007; Zhang et al., 2017). Two-month PM concentration
138 data from Beijing in the winter of 2018 were collected. As expected, during this time,
139 Beijing experienced severe and frequent haze pollution episodes with two heavy
140 episodes in which the maximum hourly $PM_{2.5}$ concentration reached ~200 μg m^{-3} and
141 six moderate episodes in which the $PM_{2.5}$ mass concentration ranged from ~100-150
142 μg m^{-3} (Figure S2a).
143 Although the air pollution process is variable and complicated, it is worth stating
144 that Beijing's haze pollution in winter can be generally classified as two kinds of
145 patterns, as shown in Figure S2b. For all haze episodes ①-⑦, the $PM_{2.5}$ mass
146 concentration slowly increased in the afternoon of the 1st day, followed by a
147 secondary maximum in the early morning and a maximum at midnight of the 2nd day.
148 In comparison to the processes of ④-⑦, where the $PM_{2.5}$ mass concentration sharply
149 decreased to <25 μg m^{-3} in the early morning of the 3rd day, during periods ①-③,
150 however, the highest $PM_{2.5}$ mass concentration (~100-200 μg m^{-3}) was observed on
151 the whole 3rd day, which disappeared on the 4th day. As previously reported,

transport, chemical transformation and boundary layer structure (local meteorological conditions) are central to determining the amount and type of pollutant loading. Considering the equivalent emission and transport effects, the suspended particles in ④-⑦ subjected to diffuse would be controlled by the atmospheric motion (wind and turbulence) on the 3rd day. The particles during periods ①-③ continuing to accumulate were therefore highly related to the specific ABL status. To investigate the possible reasons for the different variation trends of haze episodes ①-③ and ④-⑦, in the next section, we will mainly focus on the ABL structure (local meteorological conditions) influences.

3.2. Qualitative analysis of the interaction between particulate matter and boundary layer structure

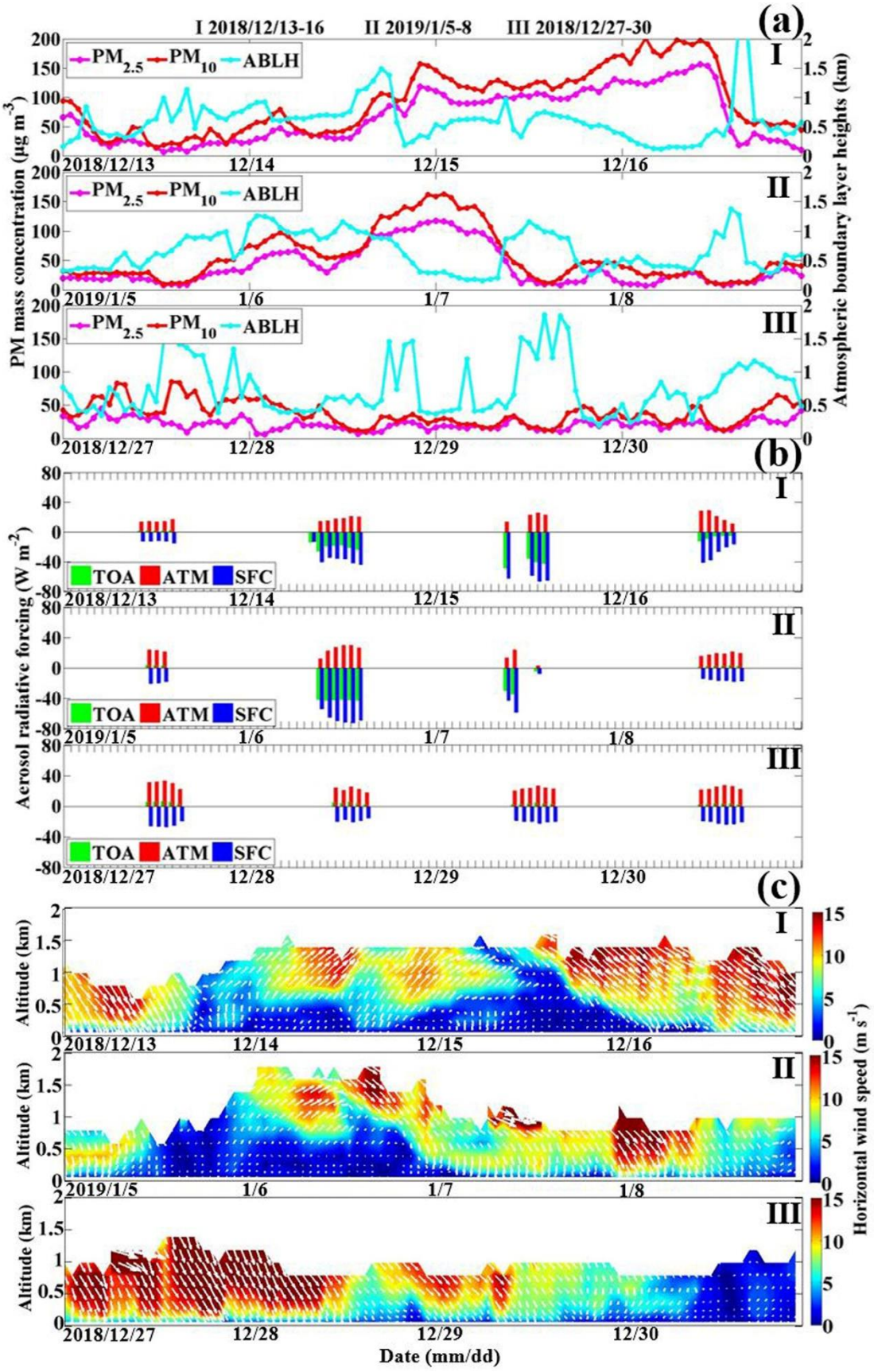

163 Figure 1. Temporal evolution of (a) the PM mass concentration and atmospheric

boundary layer height ($PM_{2.5}$: solid pink lines; PM_{10}: solid red lines; ABLH: solid blue lines), (b) aerosol radiative forcing at the top (TOA; green bars), surface (SFC; blue bars) and interior of the atmospheric column (ATM; red bars), and (c) horizontal wind vector profiles (shaded colors: wind speeds; white arrows: wind vectors) during the typical haze pollution episodes of I (2018/12/13-16) and II (2019/1/5-8) as well as the typical clean period of III (2018/12/27-30).

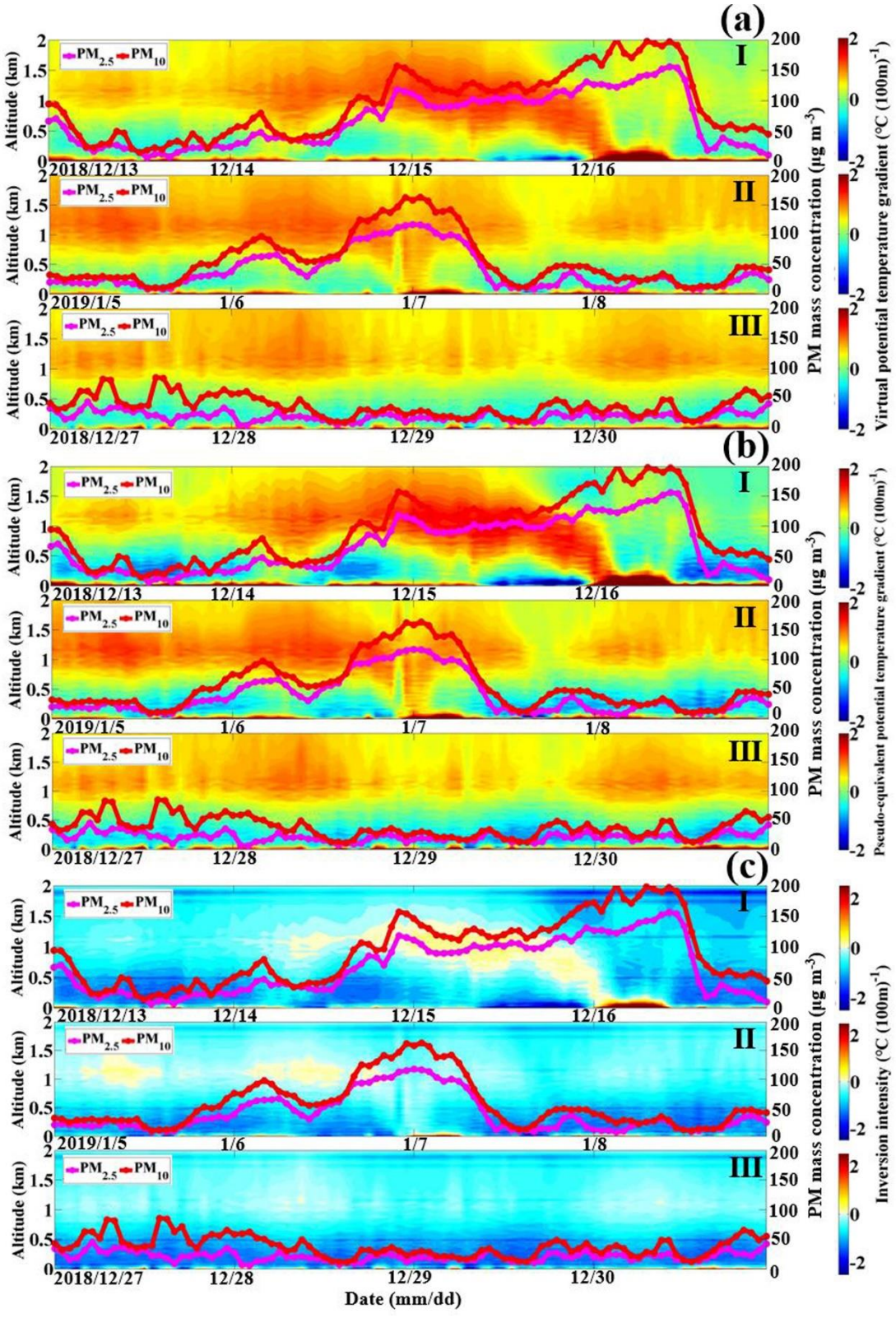

Figure 2. Temporal variation in the vertical profiles of (a) the virtual potential temperature gradient ($\partial\theta v/\partial z$), (b) pseudoequivalent potential temperature gradient ($\partial\theta se/\partial z$) and (c) temperature inversion phenomenon (shaded colors: inversion

intensity) during the typical haze pollution episodes of I (2018/12/13-16) and II (2019/1/5-8) as well as the typical clean period of III (2018/12/27-30).

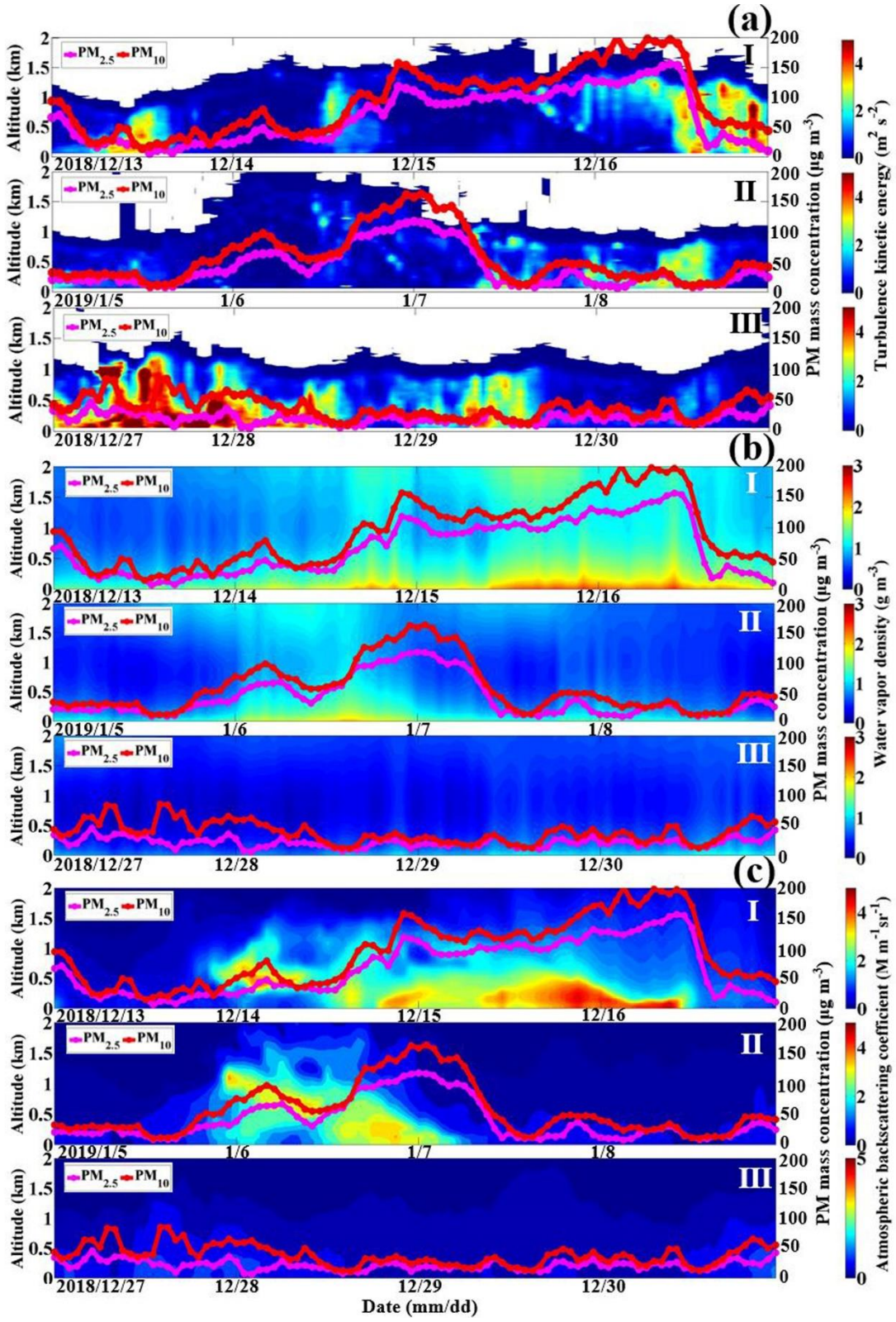

Figure 3. Temporal variation in the vertical profiles of (a) the turbulent activity

178 (shaded colors: TKE), (b) atmospheric humidity (shaded colors: vapor density), and
179 (c) vertical distribution of suspended particles (shaded colors: BSC) during the typical
180 haze pollution episodes of I (2018/12/13-16) and II (2019/1/5-8) as well as the typical
181 clean period of III (2018/12/27-30).

182 The haze episodes in winter in Beijing basically followed two different kinds of
183 variation patterns as described in the previous section. The specific reason for this
184 finding will be systematically analyzed in this section. To better illustrate the two
185 different haze patterns, a typical clean period will be considered a control. The typical
186 air pollution episodes I (E-I) (13-16 December 2018) and II (E-II) (5-8 January 2019),
187 as well as the typical clean episode III (E-III) (27-30 December 2018), are chosen as
188 examples for analysis.

189 *a. Similar change trends in the first two days*

190 Numerous studies have reported that PM's original explosive growth is caused
191 by pollution transport under southerly winds (Ma et al., 2017; Zhao et al., 2019;
192 Zhong et al., 2018). In this study, the action of southerly winds on the air pollution in
193 Beijing was presented more clearly as the Windcube 100s lidar obtained the
194 distribution of the horizontal wind vectors extending to heights of 1-1.5 km
195 (equivalent to the entire ABL) (Figure 1c). On the 1st day of E-I and E-II, the
196 atmosphere layer up to ~1 km in height was controlled by strong and clean north
197 winds, exactly like clean E-III. No pollution transport occurred, and the PM and ARF
198 levels were equivalent to those on a clean day (Figures 1a-b). The atmospheric
199 backscattering coefficients throughout the ABL during the three episodes only ranged

from ~0-1.5 M m^{-1} sr^{-1} (Figure 3c). From the evening of the 1st day to the forenoon of the 2nd day, strong southerly winds blew across Beijing during both E-I and E-II, with the wind speed reaching ~5-15 m s^{-1} at an atmosphere of about 0.5-1.5 km, while north winds still dominated the ABL during clean E-III. Sensitive to the change in wind direction from north to south, the PM concentration progressively increased from a fairly low level to ~50 μg m^{-3}. Moreover, the BSCs sharply increased to ~3 Mm^{-1} rd^{-1} and were concentrated at altitudes from ~0.5-1 km, which further stressed the effects of southerly transport on the PM concentration's original growth over Beijing. With prevailing winds originating from the wetter south, compared to the low humidity during clean E-III, the air humidity in Beijing during this time also increased, with the vapor density ranging from ~1.5-2 g m^{-3} for both E-I and E-II (Figure 3b).

At midnight of the 2nd day, the PM concentration reached its highest level with a $PM_{2.5}$ (PM_{10}) concentration of ~110 (150) μg m^{-3} during both E-I and E-II. Meanwhile, the highest BSC values mainly occurred from the ground to a height of 1 km at this time, implying that a portion of the suspended particles was pushed down to the near-surface. Before southerly wind transport occurred, the evolution of the stability indicator ($\partial\theta_v/\partial z$; $\partial\theta_{se}/\partial z$) profiles during E-I and E-II was analogous to that during clean E-III (Figures 2a-b). The stratification states at the different heights (0-1 km) were either unstable or neutral, with negative or zero $\partial\theta_v/\partial z$ values, respectively, whereby no clear nor strong temperature inversion phenomenon occurred in the boundary layer (Figure 2c). And the corresponding ABLHs were the same (Figure 1a).

However, the atmospheric stratification from ~0.5-1 km during E-I and from 0-1 km during E-II became quite stable at night of the 2nd day, with positive values of $\partial\theta_{se}/\partial z$ and weak turbulent activity (TKE: ~0 m^2 s^{-2}) (Figure 3a). In contrast to an increased ABLH during clean E-III, the ABLHs during E-I and E-II sharply decreased. Considering strong aerosol scattering and absorbing radiation could affect the temperature stratification (Li et al., 2010; Zhong et al., 2018a). With the elevated PM level due to southerly transport during E-I and E-II, ARF increased as expected with SFC (ATM) reaching ~-40 (~20) W m^{-2} and ~-75 (~30) W m^{-2}, respectively. Besides, TOA has an analogous variation trend with SFC, increasing from relatively low values to ~-20 W m^{-2} and ~-45 W m^{-2}, respectively. Therefore, less radiation reached the ground and more heated the atmosphere above the ground during E-I and E-II, and in comparisons with clean E-III, the atmospheric stratification was altered and the stability was thus increased at night. The suspended particles brought by southerly transport originally occurring at high altitudes were restrained from vertically spreading and gradually sank due to gravity and accumulated near the surface.

b. Different change trends in the next two days

It is salient to note that the haze evolution trends during E-I and E-II were consistent so far, corresponding to a similar ABL structure. Nevertheless, the north winds (~10-15 m s^{-1}) during E-II, which only blew above the ABL (>1 km) at midnight of the 2nd day, gradually spread downward and controlled the whole boundary layer on the 3rd day. The wind field is critical concerning horizontal dispersion in the boundary layer; thus, the strong, clean and dry north winds during E-

II greatly diffused the already accumulated particles first, where the $PM_{2.5}$ mass concentration decreased from ~100 to ~50 μg m^{-3}. The ARF obtained at 9:00 sharply decreased compared to yesterday, and with solar radiation heating the ground in the morning on the 3rd day, the development of daytime mixing layer eliminated the previous night's temperature structure. The temperature stratification became similar to that on clean E-III with a similar increase in ABLH. An unstable/neutral atmospheric state with a TKE of ~2 m^2 s^{-2} was also conducive to the vertical spread of substances. In response, the PM concentration (BSC) and air humidity during E-II gradually decreased with the convective boundary layer development and reached the same level as those during clean E-III.

Different from E-II, in which clean and strong north winds in the 3rd daytime contributed to the diffusion of previous night's stable stratification, there were still south winds in E-I, which once filled the boundary layer on the 2nd day, gradually decelerated over time from the ground to high altitudes. The atmosphere layer with calm/light winds extended from the ground to the height of ~1.0 km in the 3rd daytime and gradually down to the height of ~0.2 km at midnight and the forenoon of the 4th day. Due to the maintaining high PM levels, SFC and TOA further increased, up to ~-40 W m^{-2} and ~-75 W m^{-2}, respectively, with ATM remaining high (~25 W m^{-2}), which facilitated the temperature inversion that lasted from the whole 3rd day to the noon of the 4th day. As shown in Figure 2(a-c)-I, there was continue temperature inversion structure from ~0.5-1.0 km altitude and the atmospheric stratification was quite stable on the 3rd daytime and at midnight. Since the temperature inversion layer

acted as a lid at altitudes of ~0.5-1.0 km, downward momentum transport would be blocked. Original south winds near the ground were constantly consumed by friction, further explaining the lower atmosphere layer's calm/light winds. With quite strong north winds started blowing at high altitude at the 3rd night and surface cooling strengthening, the temperature inversion at ~0.5-1.0 km was gradually broke and turned to ground-touching temperature inversion at 0-0.2 km altitude at midnight. This abnormal temperature structure lasted till noon of the 4th day, mainly due to the strong aerosol direct radiation effect of the pre-existing high PM level. As expected, we can see the strong north winds above ~1.0 km at the 3rd night gradually extended downward and eventually occurred above the ground-touching inversion in the forenoon of the 4th day. Therefore, with calm/light winds and weak turbulent activity below the temperature inversion in the 3rd day, the PM concentrated exactly below the inversion lid (below ~0.5 km) and maintained high concentrations, as the BSC distribution shows in Figure 3c-I. With strong ground-touching inversion of 0-0.2 km altitude forming at midnight and the forenoon of the 4th day, the accumulated particles near the surface were further inhibited right in the stable atmosphere layer (below ~0.2 km). The same effect was exerted on the water vapor so as to the high air humidity below the inversion lid at this time. Therefore, the pollutant layer was compressed downward accompanied by intense heterogeneous hydrolysis reactions at the moist particle surface (Zhang et al., 2008), thus resulting in the continue increase of near-surface $PM_{2.5}$ concentrations. At noon of the 4th day, the north winds further accelerated with wind speed higher than ~15 m s^{-1} and spread down to the whole

ABL, which promoted the horizontal and convective dispersion of pollutants and water vapor, and the PM mass concentration, therefore, dropped to the same level as that on clean E-III. With $PM_{2.5}$ sharply dropped from ~150 μg m^{-3} to ~20 μg m^{-3} in four hours, the aerosol direct radiation effect was sensitive to PM changes and gradually decreased from 10:00 to 14:00, reaching the same level as those on clean E-III finally.

In this section, through a detailed contrastive analysis, we examined the potential reasons for the occurrence of the two different patterns of haze pollution in winter in Beijing. We found that the crucial point in determining whether the PM mass concentration remained high or sharply decreased was related to whether the boundary layer remained stable. The boundary layer stability was, in turn notably linked to the PM mass concentration and aerosol direct radiation effect.

3.3. Quantitative analysis of the effect of particulate matter on the boundary layer structure

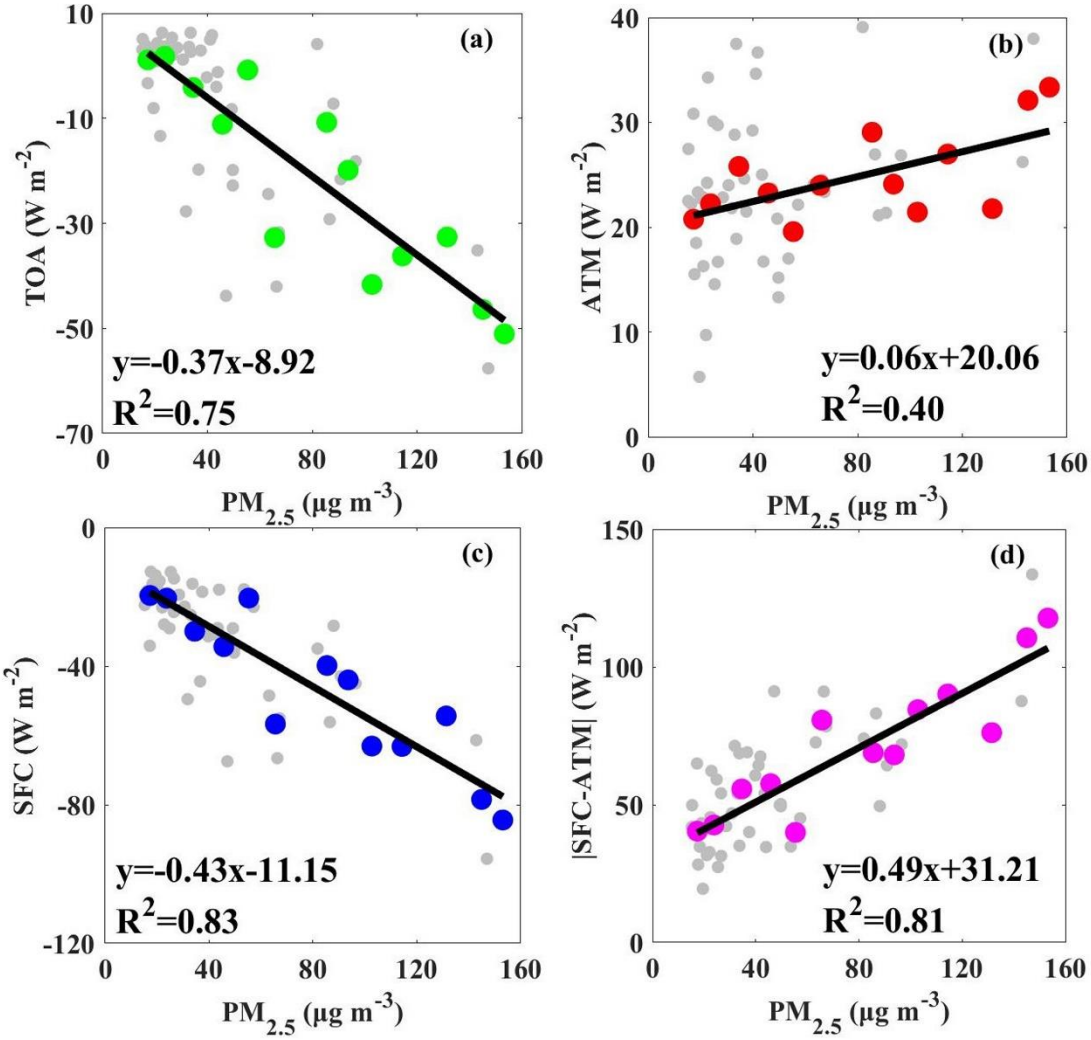

Figure 4. Scatter plots of the $PM_{2.5}$ mass concentration (x) versus aerosol radiative forcing at the top of the atmospheric column (TOA; y; a), the interior of the atmospheric column (ATM; y; b), and the surface (SFC; y; c) as well as the absolute difference of SFC and ATM (|SFC-ATM|; y; d), respectively (gray dots: daily data; other dots: mean data). (The daily data means daily mean values of TOA, ATM, SFC, and corresponding daily averaged $PM_{2.5}$ mass concentration from 27 November 2018 to 25 January 2019 in Beijing. The mean $PM_{2.5}$ concentrations were obtained by averaging daily $PM_{2.5}$ concentrations at intervals of 10 μg m^{-3}. The mean TOA, ATM, and SFC were obtained after the corresponding daily TOA, ATM, and SFC average,

312 respectively. For example, all daily $PM_{2.5}$ concentrations greater than 40 μg m^{-3} and
313 less than 50 μg m^{-3} were averaged as a mean $PM_{2.5}$ concentration, and TOA values
314 (ATM; SFC) corresponding to this daily $PM_{2.5}$ concentration range were also averaged
315 as a mean TOA (ATM; SFC)).

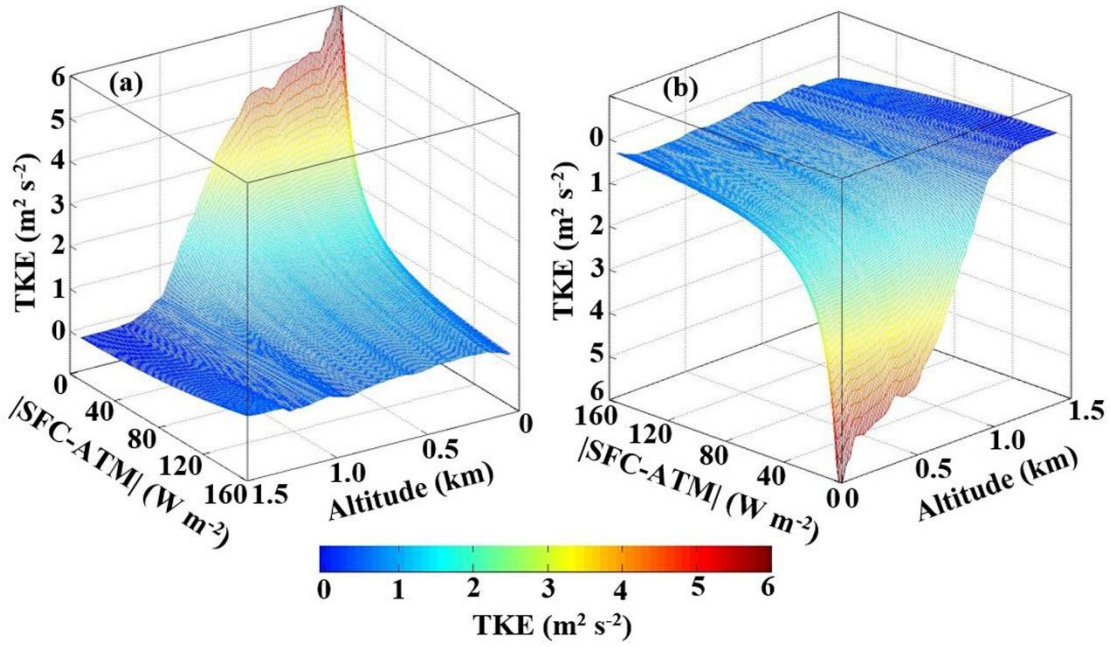

316

317 Figure 5. 3-D plot of the fitting relationship of the absolute difference in aerosol
318 radiative forcing between the surface and interior of the atmospheric column (|SFC-
319 ATM|; *x*) and turbulence kinetic energy (TKE; *z*) at the different altitudes (*y*) ((a) and
320 (b) present different perspectives).

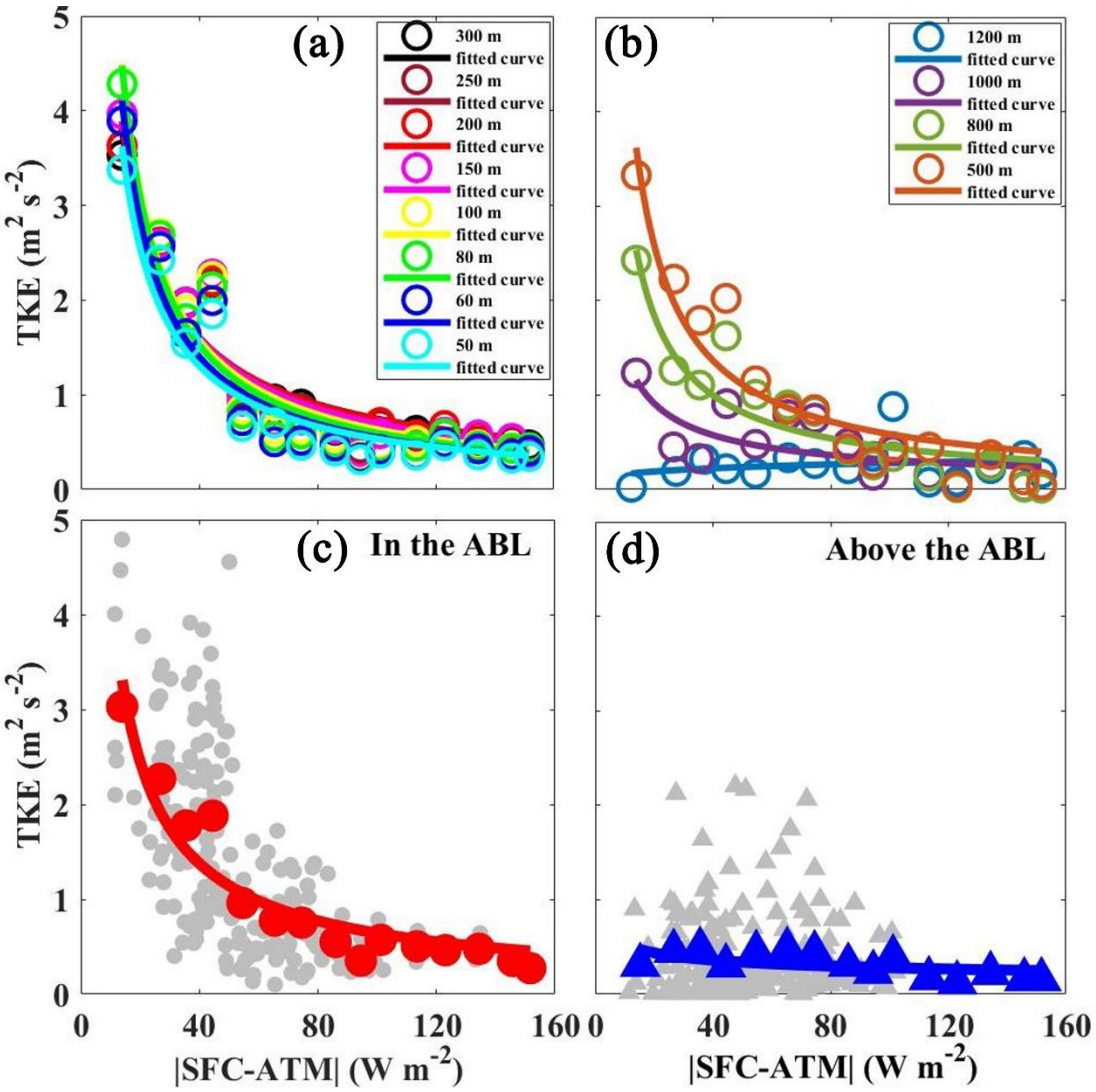

321

322 Figure 6. Scatter plots of the mean absolute difference of the aerosol radiative forcing

323 at the surface and interior of the atmospheric column (|SFC-ATM|; x) versus the mean

324 turbulence kinetic energy (TKE; y) at the different altitudes (a; b). Scatter plots of

325 |SFC-ATM| (x) versus TKE (y) in the ABL (c) and above the ABL (d) (gray dots:

326 hourly data; other dots: mean data). The hourly data were collected over a two-month

327 period in Beijing from 27 November 2018 to 25 January 2019. (The hourly data

328 means hourly mean values of |SFC-ATM| and corresponding hourly TKE. The mean

329 |SFC-ATM| was obtained by averaging hourly |SFC-ATM| at intervals of 10 W m^{-2},

330 then the mean TKE was obtained after the average of the corresponding hourly TKE.).

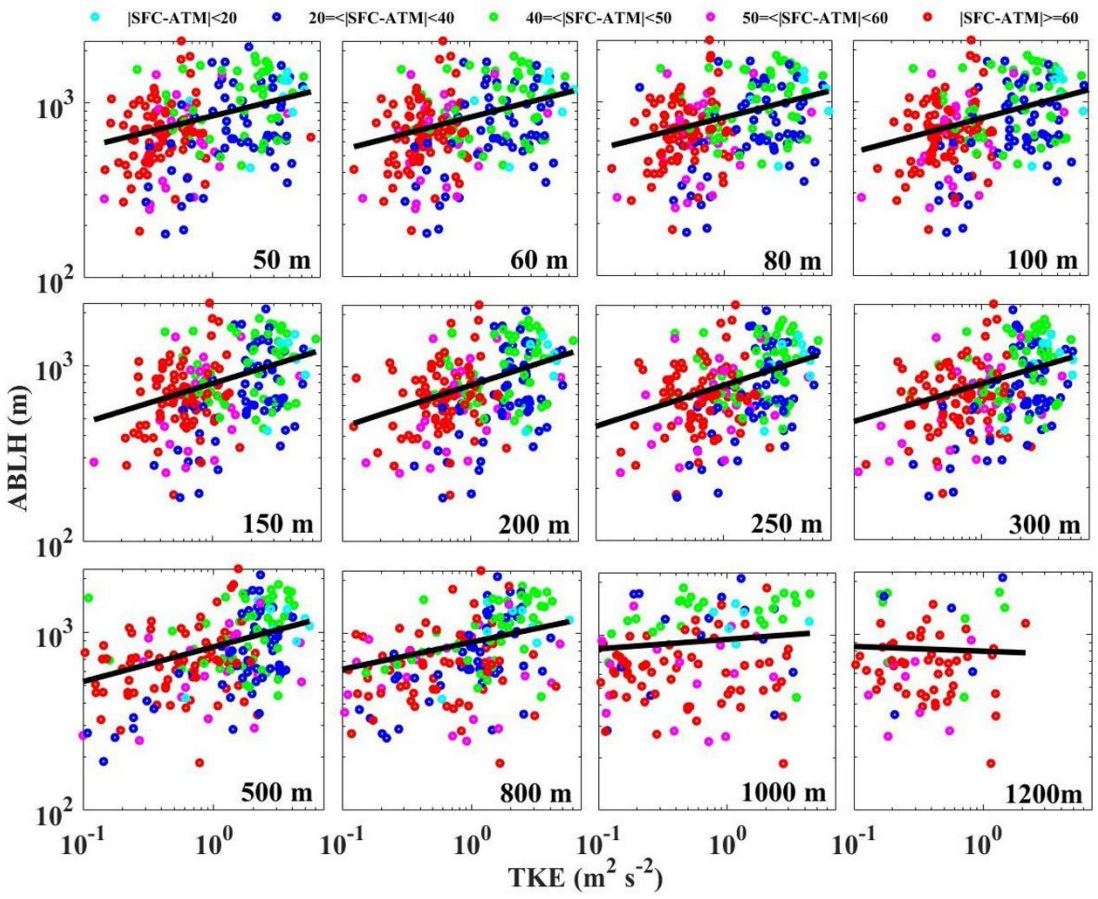

Figure 7. The atmospheric boundary layer height (ABLH; y) as a function of the turbulence kinetic energy (TKE; x) at the different altitudes and the aerosol direct radiation effect defined as |SFC-ATM| (color code). The calculated hourly data used above are collected over two months in Beijing from 27 November 2018 to 25 January 2019.

Based on the contrastive analysis in the previous section, it was clear that the ABL structure played a critical role in the maintenance and dissipation of air pollution. It appeared that the increase in atmospheric stability suppressed pollution diffusion under a weak turbulence activity and low ABLH. Water vapor also significantly accumulated to a relatively high level near the surface, further facilitating secondary aerosols' formation. The evolution of ABL stability essentially

occurred in response to the atmospheric temperature structure, as analyzed above, which was influenced by the strong aerosol direct radiation effect (Andrews, 2000; Li et al., 2010). The Archimedes buoyancy generated by the pulsating temperature field in the gravity field exerted negative work on the turbulent pulsating field with a stable ABL occurring. The turbulence served as a carrier for substance transport in the boundary layer, such as water vapor, heat, and PM (Garratt et al., 1992). Thus, in the following section, the ARF and TKE were chosen as the key parameters to examine how PM affects and modifies the boundary layer structure.

Figure 4 shows the relationship between the PM concentration and ARF. As shown in Figures 4a and 4c, TOA and SFC were proportional to the $PM_{2.5}$ concentration, respectively. With the increase in $PM_{2.5}$ concentration, elevated aerosol loading near the surface would scatter more solar radiation back into outer space and cause less solar radiation reaching the ground, corresponding to a cooling of the surface and making negative SFC. TOA means the aerosol radiative forcing at the top of the atmosphere column and is the sum of ATM and SFC. Considering that anthropogenic aerosols are mostly scattering aerosols, the SFC forcing is generally stronger than ATM, corresponding to a cooling of the earth-atmosphere system. The TOA forcing was thus usually negative and had a similar trend with SFC. ATM, driven by aerosol absorption effect and representing a warming effect of aerosols on the atmosphere layer, exhibited a positive correlation with the $PM_{2.5}$ concentration (see Figure 4b). These results demonstrated that a higher $PM_{2.5}$ concentration would arouse a stronger ARF, further inhibiting solar radiation from reaching the ground and

heating the atmosphere layer more. |SFC-ATM|, defined as the absolute value of the difference between SFC and ATM, represents aerosols' combined action on the solar radiation reaching the aerosol layer and the ground. Larger values of |SFC-ATM| indicate stronger aerosol scattering and/or absorption effects, further implying a more significant temperature difference between the ground and the above atmosphere layer. As expected, a positive linear correlation between |SFC-ATM| and $PM_{2.5}$ concentration was found, as shown in Figure 4d.

As described in the above paragraph, there was a strong ARF under a high PM loading, which markedly altered the atmospheric temperature structure, further changing the ABL structure. It is necessary to determine the effect degree of ARF on the boundary layer structure. Figure 5 shows the 3-D plots of the fitting relationship between the hourly values of |SFC-ATM| and TKE at the different altitudes. What stood out in Figure 5a was the general decline in TKE concerning the growth of |SFC-ATM|. With increasing |SFC-ATM| value, the TKE value at the different altitudes always decreased exponentially and approached zero below ~0.8 km. The notable exponential function between TKE and |SFC-ATM| explained that a strong ARF would drastically change the boundary layer into highly stable conditions characterized by a rather low TKE. The results above highlight the aerosol direct radiation effect' s nonnegligible impact on the boundary layer structure, especially during the haze episode under a high aerosol loading with a strong ARF. It is well known that a larger net negative/positive SFC/ATM arises a cooler/warmer ground/atmosphere. An increase in |SFC-ATM| implies the gradual intensification of

387 the ground cooling and/or atmosphere heating processes. Therefore, it changed the
388 atmospheric stratification into a gradually enhanced stable state, which was
389 characterized by increasingly weaker turbulence activities. Additionally, as shown in
390 Figure 5b, we can identify a critical point of the |SFC-ATM| effects on TKE in the low
391 layers. In particular, TKE decreased with increasing |SFC-ATM| and hardly changed
392 when |SFC-ATM| exceeded the critical point.

393 To define the critical point, we generated scatter plots of the average |SFC-ATM|
394 and TKE at different altitudes, as shown in Figures 6a-b. The scatter plots of the
395 unaveraged hourly data are shown in Figure S3, and the fitting functions are listed in
396 Table S1. Depending on the exponential curve's maximum curvature (Silvanus and
397 Gardner, 1998), a critical point should exist. With the mean TKE and |SFC-ATM|
398 values on the exponential curve, we found that once the aerosol direct radiation effect
399 defined by |SFC-ATM| exceeded 50-60 W m^{-2} (average of ~55 W m^{-2}), the TKE
400 sharply decreased from ~2 m^2 s^{-2} to lower than 1 m^2 s^{-2}. This means that a high aerosol
401 loading with a |SFC-ATM| value higher than ~55 W m^{-2} tends to change the boundary
402 layer from the unstable state to the extremely stable state in a short time, and further
403 increasing |SFC-ATM| would barely modify the ABL structure. The average |SFC-
404 ATM| value of ~55 W m^{-2} can be defined as the threshold of the ARF effects on the
405 ABL structure, which could provide useful information for relevant model
406 simulations, atmospheric environment improvement measures, and relevant policies.
407 Besides, as shown in Figures 5-6, the exponential relationship between TKE and
408 |SFC-ATM| was notable in the low layers and gradually deteriorated with increasing

altitude. On average, the exponential relationship was notable in the ABL and almost disappeared above the ABL (Figures 6c-d). Considering that aerosols are mainly concentrated below the lower atmosphere, contributing the most to the SFC and ATM forcing, which further confirmed that the considerable change in atmospheric stratification caused by aerosols existed and mainly occurred in the lower layers.

The previous discussion shows that a strong aerosol direct radiation effect markedly affected the turbulent activity and modified the boundary layer structure. As many studies have reported, the ABLH is an important meteorological factor that influences the vertical diffusion of atmospheric pollutants and water vapor (Stull, 1988; Robert and Aron, 1983). The following examines the relationship among the turbulent activity, ARF, and ABLH to illustrate the change in ABLH in response to ARF. Figure 7 shows the ABLH as a function of the TKE and |SFC-ATM| at the different altitudes. It was apparent that a positive correlation exists between TKE and ABLH. As the turbulent activity became increasingly weaker, the corresponding boundary layer height gradually decreased, responding to the gradual increase in |SFC-ATM|. Similar to the relationship between the turbulent activity and aerosol radiative effect, as shown in Figure 6, the relationship among these aspects was much stronger below 300 m and almost disappeared above 800 m. This further addressed the fact that the change in boundary layer height was attributed to the turbulence activity variation stemming from the aerosol direct radiation effect.

Thus far, this section has demonstrated that the aerosol loading with aerosol radiative effects impacted the turbulent activity, changed the boundary layer height,

and modified the boundary layer structure. On the other hand, it is now necessary to explain how the renewed boundary layer structure modifies the $PM_{2.5}$ concentration. As shown in Figures S4a-b, the ABLH as an independent variable impact the ambient water vapor in the ABL to some degree. There was a steady increase in the ambient humidity with decreasing ABLH, where absolute humidity (AH) and relative humidity (RH) were projected to decrease to ~3 g m^{-3} and ~60%, respectively, with the ABLH decreasing below ~500 m. With the increase in ambient humidity, a marked rise in $PM_{2.5}$ concentration occurred, as shown in Figures S4c-d. Once AH and RH exceeded ~3 g m^{-3} and ~60%, respectively, the $PM_{2.5}$ concentration reached ~100 μg m^{-3}. The results above indicate that with a fairly low boundary layer height, water vapor accumulated near the surface, and particles tended to hygroscopic grow, resulting in secondary aerosol formation in a high-humidity environment, further increasing the $PM_{2.5}$ concentration. As shown in Figure S4e, with the level off of the ABLH, the $PM_{2.5}$ mass concentration increased exponentially and reached a high value. The exponential relationship was similar to that between the ambient humidity and ABLH, which revealed that the explosive growth of the $PM_{2.5}$ concentration under a low ABLH was largely driven by intense secondary aerosol formation and hygroscopic growth at high ambient humidity.

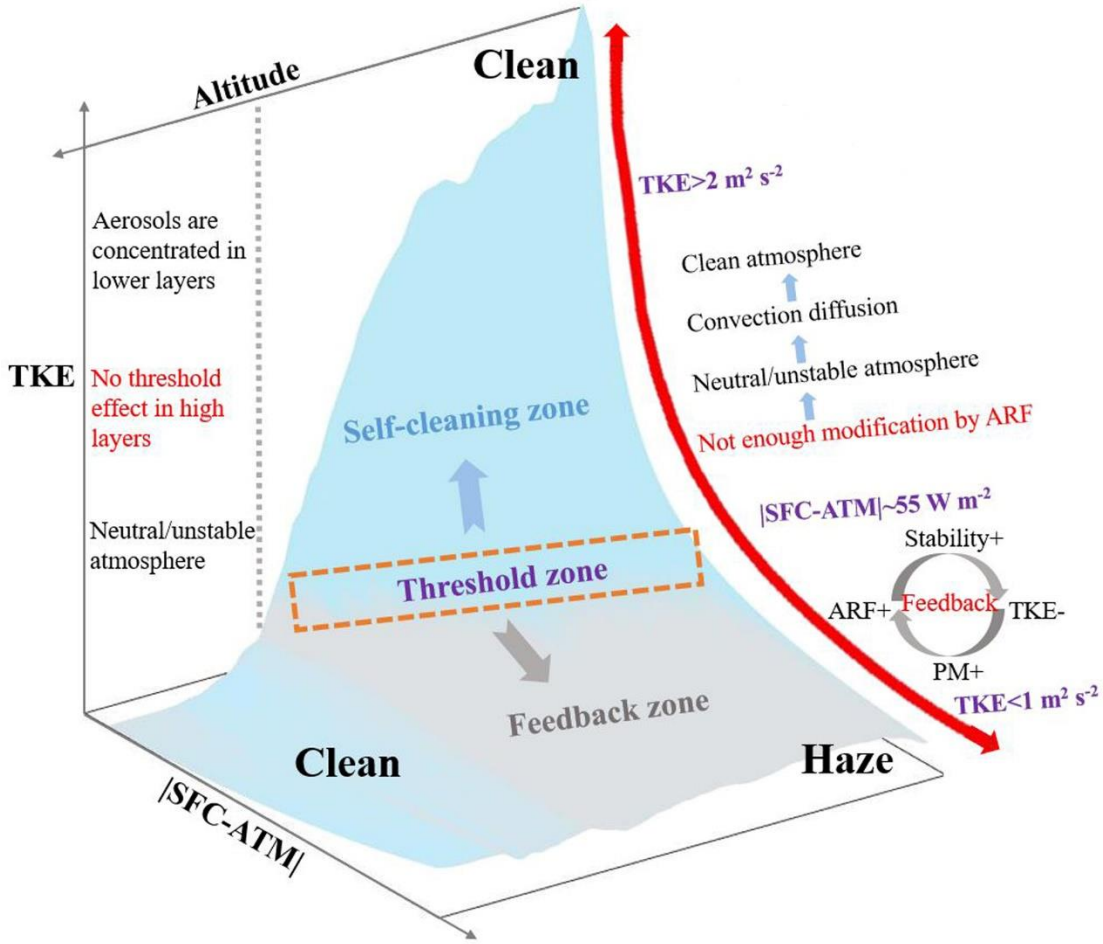

Figure 8. Schematic diagram of the interaction between the aerosol radiative forcing (ARF) and boundary layer structure (|SFC-ATM|: the mean absolute difference of the aerosol radiative forcing at the surface and interior of the atmospheric column; TKE: the mean turbulence kinetic energy).

4. Conclusion

By analyzing the two-month haze conditions in winter in Beijing, we found that haze pollution basically underwent two different variation patterns, namely, the same trends on the first two days, and on the next days, one haze pattern went through a continuing outbreak, while the other haze pattern exhibited notable diffusion. Considering equivalent emissions, this has raised important questions about whether and how the local boundary layer structure impacted/caused this difference. The

results of a contrastive analysis qualitatively showed that the crucial point in determining whether the PM concentration remained very high or sharply decreased was largely related to whether the boundary layer structure (i.e., stability and TKE) satisfied relevant conditions. As previous studies reported (Liu et al., 2018; Zhong et al., 2018b; Zhong et al., 2019) and was confirmed in this paper, the extremely stable stratification with positive $\partial\theta_{se}/\partial z$ values and a low TKE was the premise of the outbreak of haze pollution. However, the change/state of the boundary layer structure was, in turn, strongly linked to the PM mass concentration and ARF, and we further quantitatively evaluated the effect of ARF on the boundary layer structure. Figure 8, emerging from the previous observation analysis, is where ARF modifies the boundary layer structure and aggravates haze pollution. The ARF effects on the atmospheric stratification depend on the reduced radiation reaching the ground due to aerosol scattering and absorbing radiation in the atmosphere (Dickerson et al., 1997; Stone et al., 2008). Firstly, we found that a positive linear relationship between |SFC-ATM| and $PM_{2.5}$ concentration existed, which means the strong aerosol scattering and/or absorption effect occurs during the heavy haze episodes and could arouse significant temperature differences between the surface and the above atmosphere layer. Secondly, previous studies revealed that black carbon solar absorption suppresses turbulence near the surface (Wilcox et al., 2016); while we found that the TKE value at the different altitudes always decreased exponentially with increasing |SFC-ATM|, which was significant in the lower atmosphere layer. Moreover, the ARF effects on turbulent activity were found significant in the boundary layer and

disappeared above the boundary layer, which also confirmed that the stronger ARF from the aerosol layer would indeed change the boundary layer into the considerably stable state characterized by a relatively low TKE. Thirdly, the ARF change is linear due to the PM concentration; however, the influence of ARF on the boundary layer structure is nonlinear. Based on the exponential relationship, the threshold of the ARF effects on the boundary layer structure has been determined for the first time, highlighting that once the ARF exceeded a specific value, the boundary layer structure tends to quickly stabilize after that changed little with increasing ARF. This threshold could provide useful information for relevant atmospheric environment improvement measures and policies in Beijing. When the $PM_{2.5}$ concentration is controlled with the ARF below the threshold, the unstable atmosphere's self-purification capacity could effectively dilute and diffuse pollutants. In contrast, when the $PM_{2.5}$ concentration increases with an ARF exceeding the threshold value, the boundary layer would stabilize sharply, especially in the lower layers, aggravating haze pollution.

Data availability

The surface $PM_{2.5}$ & PM_{10} and other trace gases observation data used in this study can be accessed from http://106.37.208.233:20035/ (last access: 4 June 2020). Other datasets can be accessed upon request to the corresponding author.

Author contribution

XJ designed the experiments and the research. ZD, GC, QJ, WY, TG, MY, DL, WX, LG, MY provided experimental assistance and analytical method. ZD and XJ analyzed the data and performed research. All authors commented on the manuscript.

Competing interests

The authors declare that they have no conflict of interest.

Acknowledgments

This study was supported by the Ministry of Science and Technology of China (grant number 2016YFC0202001), the CAS Strategic Priority Research Program (XDA23020301), and the National Natural Science Foundation of China (grant number 42061130215). The authors are thankful for the data support from the Ministry of Ecology and Environment of the People's Republic of China, the National Earth System Science Data Sharing Infrastructure, National Science and Technology Infrastructure of China (available at http://www.geodata.cn, last access: 4 June 2020).

References

An, Z., Huang, R.-J., Zhang, R., Tie, X., Li, G., Cao, J., Zhou, W., Shi, Z., Han, Y., Gu, Z., and Ji, Y.: Severe haze in northern China: A synergy of anthropogenic emissions and atmospheric processes, Proc. Natl. Acad. Sci. U. S. A., 116, 8657-8666, https://doi.org/10.1073/pnas.1900125116, 2019.

Andrews, D. G.: An Introduction to Atmospheric Physics, Cambridge University Press, 2000.

Barbaro, E., Arellano, J., Ouwersloot, H., Schröter, J., Donovan, D., and Krol, M.: Aerosols in the convective boundary layer: Shortwave radiation effects on the coupled land‐atmosphere system, J. Geophys. Res.: Atmos., 119, 5845–5863, https://doi.org/10.1002/2013JD021237, 2014.

Dickerson, R. R., Kondragunta, S., Stenchikov, G., Civerolo, K. L., Doddridge, B. G., and Holben, B. N.: The impact of aerosols on solar ultraviolet radiation and photochemical smog, Science (New York, N.Y.), 278, 827-830, https://doi.org/10.1126/science.278.5339.827, 1997.

Garratt, J. R., Dessler, A. J., Houghton, J. T., and Rycroft, M. J.: The atmospheric boundary layer, 1992.

Ding, A., Huang, X., Nie, W., Sun, J., Kerminen, V.‐M., Petäjä, T., Su, H., Cheng, Y., Yang, X., Wang, M., Chi, X., Wang, J., Virkkula, A., Guo, W., Yuan, J., Wang, S., Zhang, R., Wu, Y., Song, Y., Zhu, T., Zilitinkevich, S., and Kulmala, M.: Enhanced haze pollution by black carbon in megacities in China, Geophys. Res. Lett., 43, 2873–2879, https://doi.org/10.1002/2016GL067745, 2016.

Gong, C., Xin, J., Wang, S., Wang, Y., Wang, P., Wang, L., and Li, P.: The aerosol direct radiative forcing over the Beijing metropolitan area from 2004 to 2011, J. Aerosol Sci., 69, 62-70, https://doi.org/10.1016/j.jaerosci.2013.12.007, 2014.

Gregory, L.: Cimel Sun-photometer (CSPHOT) Handbook, 2011.

Guo, S., Hu, M., Zamora, M. L., Peng, J., Shang, D., Zheng, J., Du, Z., Wu, Z., Shao, M., Zeng, L., Molina, M. J., and Zhang, R.: Elucidating severe urban haze formation in China, Proc. Natl. Acad. Sci. U. S. A., 111, 17373-17378,

https://doi.org/10.1073/pnas.1419604111, 2014.

Haman, C. L., Couzo, E., Flynn, J. H., Vizuete, W., Heffron, B., and Lefer, B. L.: Relationship between boundary layer heights and growth rates with ground-level ozone in Houston, Texas, J. Geophys. Res.: Atmos., 119, 6230-6245, https://doi.org/10.1002/2013jd020473, 2014.

Han, S., Bian, H., Tie, X., Xie, Y., Sun, M., and Liu, A.: Impact of nocturnal planetary boundary layer on urban air pollutants: Measurements from a 250-m tower over Tianjin, China, J. Hazard. Mater., 162, 264-269, https://doi.org/10.1016/j.jhazmat.2008.05.056, 2009.

Hua, Y., Wang, S., Wang, J., Jiang, J., Zhang, T., Song, Y., Kang, L., Zhou, W., Cai, R., Wu, D., Fan, S., Wang, T., Tang, X., Wei, Q., Sun, F., and Xiao, Z.: Investigating the impact of regional transport on PM2.5 formation using vertical observation during APEC 2014 Summit in Beijing, Atmos. Chem. Phys., 16, 15451-15460, https://doi.org/10.5194/acp-16-15451-2016, 2016.

Huang, X., Wang, Z., and Ding, A.: Impact of Aerosol-PBL Interaction on Haze Pollution: Multiyear Observational Evidences in North China, Geophys. Res. Lett., 45, 8596-8603, https://doi.org/10.1029/2018gl079239, 2018.

Jin-Xiang, L. I.: The Characteristics and Cause Analysis of Heavy-Air-Pollution in Autumn and Winter in Beijing, Environ. Monit. China, 2007.

Kotthaus, S., and Grimmond, C. S. B.: Atmospheric boundary-layer characteristics from ceilometer measurements. Part 1: A new method to track mixed layer height and classify clouds, Q. J. R. Meteorol. Soc., 144, 1525-1538, https://doi.org/10.1002/qj.3299, 2018.

Lee K., Li Z., Wong M., Xin J., Wang Y., Hao W., and Zhao F.: Aerosol single scattering albedo estimated across China from a combination of ground and satellite measurements, J. Geophys. Res.: Atmos., 112(D22), https://doi.org/10.1029/2007JD009077, 2007.

Levy, R. C., Remer, L. A., and Dubovik, O.: Global aerosol optical properties and application to Moderate Resolution Imaging Spectroradiometer aerosol retrieval

over land, J. Geophys. Res.: Atmos., 112, https://doi.org/10.1029/2006jd007815, 2007.

Li, G., Bei, N., Cao, J., Huang, R., Wu, J., Feng, T., Wang, Y., Liu, S., Zhang, Q., Tie, X., and Molina, L. T.: A possible pathway for rapid growth of sulfate during haze days in China, Atmos. Chem. Phys., 17, 3301-3316, https://doi.org/10.5194/acp-17-3301-2017, 2017.

Li, M., Wang, L., Liu, J., Gao, W., Song, T., Sun, Y., Li, L., Li, X., Wang, Y., Liu, L., Daellenbach, K. R., Paasonen, P. J., Kerminen, V.-M., Kulmala, M., and Wang, Y.: Exploring the regional pollution characteristics and meteorological formation mechanism of $PM_{2.5}$ in North China during 2013-2017, Environ. Int., 134, https://doi.org/10.1016/j.envint.2019.105283, 2020.

Li, Z., Lee, K.-H., Wang, Y., Xin, J., and Hao, W.-M.: First observation-based estimates of cloud-free aerosol radiative forcing across China, J. Geophys. Res.: Atmos., 115, https://doi.org/10.1029/2009jd013306, 2010.

Liu, Q., Jia, X., Quan, J., Li, J., Li, X., Wu, Y., Chen, D., Wang, Z., and Liu, Y.: New positive feedback mechanism between boundary layer meteorology and secondary aerosol formation during severe haze events, Sci. Rep., 8, https://doi.org/10.1038/s41598-018-24366-3, 2018.

Liu, T. T., Gong, S., Meng, Y., Qi, C. Z., and Hong, L. L.: Contributions of meteorology and emission to the 2015 winter severe haze pollution episodes in Northern China, Atmos. Chem. Phys., 17, 1-17, https://doi.org/10.5194/acp-2016-204, 2016.

Münkel, C., Eresmaa, N., Rasanen, J., and Karppinen, A.: Retrieval of mixing height and dust concentration with lidar ceilometer, Bound.-Layer Meteorol., 124, 117-128, https://doi.org/ 10.1007/s10546-006-9103-3, 2007.

Ma, Q., Wu, Y., Zhang, D., Wang, X., and Zhang, R.: Roles of regional transport and heterogeneous reactions in the $PM_{2.5}$ increase during winter haze episodes in Beijing, Sci. Total Environ., 599-600, 246-253, https://doi.org/10.1016/j.scitotenv.2017.04.193, 2017.

Miao, Y., Guo, J., Liu, S., Zhao, C., Li, X., Zhang, G., Wei, W., and Ma, Y.: Impacts of

synoptic condition and planetary boundary layer structure on the trans-boundary aerosol transport from Beijing-Tianjin-Hebei region to northeast China, Atmos. Environ., 181, 1-11, https://doi.org/10.1016/j.atmosenv.2018.03.005, 2018.

Munro, D. S.: Boundary Layer Climatology, 2005.

Niu, F., Li, Z., Li, C., Lee, K.-H., and Wang, M.: Increase of wintertime fog in China: Potential impacts of weakening of the Eastern Asian monsoon circulation and increasing aerosol loading, J. Geophys. Res.: Atmos., 115, https://doi.org/10.1029/2009jd013484, 2010.

Petaja, T., Jarvi, L., Kerminen, V. M., Ding, A. J., Sun, J. N., Nie, W., Kujansuu, J., Virkkula, A., Yang, X. Q., Fu, C. B., Zilitinkevich, S., and Kulmala, M.: Enhanced air pollution via aerosol-boundary layer feedback in China, Sci. Rep., 6, https://doi.org/10.1038/srep18998, 2016.

Pichugina, Y. L., Banta, R. M., Bonin, T., Brewer, W. A., Choukulkar, A., McCarty, B. J., Baidar, S., Draxl, C., Fernando, H. J. S., Kenyon, J., Krishnamurthy, R., Marquis, M., Olson, J., Sharp, J., and Stoelinga, M.: Spatial Variability of Winds and HRRR-NCEP Model Error Statistics at Three Doppler-Lidar Sites in the Wind-Energy Generation Region of the Columbia River Basin, J. Appl. Meteorol. Climatol., 58, 1633-1656, https://doi.org/10.1175/jamc-d-18-0244.1, 2019.

Quan, J., Gao, Y., Zhang, Q., Tie, X., Cao, J., Han, S., Meng, J., Chen, P., and Zhao, D.: Evolution of planetary boundary layer under different weather conditions, and its impact on aerosol concentrations, Particuology, 11, 34-40, https://doi.org/10.1016/j.partic.2012.04.005, 2013.

Robert, and Aron: Mixing height—an inconsistent indicator of potential air pollution concentrations, Atmos. Environ., 17, 2193-2197, https://doi.org/10.1016/0004-6981(83)90215-9, 1983.

Schaefer, K., Wang, Y., Muenkel, C., Emeis, S., Xin, J., Tang, G., Norra, S., Schleicher, N., Vogt, J., and Suppan, P.: Evaluation of continuous ceilometer-based mixing layer heights and correlations with $PM_{2.5}$ concentrations in Beijing, in: Remote Sensing of Clouds and the Atmosphere Xiv, edited by: Picard, R. H., Schafer, K.,

Comeron, A., Kassianov, E., and Mertens, C. J., Proceedings of SPIE, 2009.

Silvanus, P. T. F. R. S., and Gardner, M.: A Little More about Curvature of Curves, Calculus Made Easy, 249-262, https://doi.org/10.1007/978-1-349-15058-8_25, 1998.

Stone, R. S., Anderson, G. P., Shettle, E. P., Andrews, E., Loukachine, K., Dutton, E. G., Schaaf, C., and Roman, M. O., III: Radiative impact of boreal smoke in the Arctic: Observed and modeled, J. Geophys. Res.: Atmos., 113, https://doi.org/10.1029/2007jd009657, 2008.

Stull, R. B.: An Introduction to Boundary Layer Meteorology, 1988.

Su, T., Li, Z., and Kahn, R.: Relationships between the planetary boundary layer height and surface pollutants derived from lidar observations over China: regional pattern and influencing factors, Atmos. Chem. Phys., 18, 15921-15935, https://doi.org/10.5194/acp-18-15921-2018, 2018.

Tang, G., Zhu, X., Hu, B., Xin, J., Wang, L., Münkel, C., Mao, G., and Wang, Y.: Impact of emission controls on air quality in Beijing during APEC 2014: lidar ceilometer observations, Atmos. Chem. Phys., 15, 12667–12680, https://doi.org/10.5194/acp-15-12667-2015, 2015.

Tang, G., Zhang, J., Zhu, X., Song, T., Muenkel, C., Hu, B., Schaefer, K., Liu, Z., Zhang, J., Wang, L., Xin, J., Suppan, P., and Wang, Y.: Mixing layer height and its implications for air pollution over Beijing, China, Atmos. Chem. Phys., 16, 2459-2475, https://doi.org/10.5194/acp-16-2459-2016, 2016.

Tie, X., Huang, R.-J., Cao, J., Zhang, Q., Cheng, Y., Su, H., Chang, D., Poeschl, U., Hoffmann, T., Dusek, U., Li, G., Worsnop, D. R., and O'Dowd, C. D.: Severe Pollution in China Amplified by Atmospheric Moisture, Sci. Rep., 7, https://doi.org/10.1038/s41598-017-15909-1, 2017.

Wang, J. Z., Gong, S. L., Zhang, X. Y., Yang, Y. Q., Hou, Q., Zhou, C. H., and Wang, Y. Q.: A Parameterized Method for Air-Quality Diagnosis and Its Applications, Adv. Meteorol., https://doi.org/10.1155/2012/238589, 2012.

Wang, X., Wei, W., Cheng, S., Li, J., Zhang, H., and Lv, Z.: Characteristics and

classification of PM 2.5 pollution episodes in Beijing from 2013 to 2015, Sci. Total Environ., 612, 170-179, https://doi.org/10.1016/j.scitotenv.2017.08.206, 2018.

Wang, Y., Yao, L., Wang, L., Liu, Z., Ji, D., Tang, G., Zhang, J., Sun, Y., Hu, B., and Xin, J.: Mechanism for the formation of the January 2013 heavy haze pollution episode over central and eastern China, Sci. China-Earth Sci., 57, 14-25, https://doi.org/10.1007/s11430-013-4773-4, 2014.

Wilcox, E. M., Thomas, R. M., Praveen, P. S., Pistone, K., Bender, F. A. M., and Ramanathan, V.: Black carbon solar absorption suppresses turbulence in the atmospheric boundary layer, Proc. Natl. Acad. Sci. U. S. A., 113, 11794-11799, https://doi.org/10.1073/pnas.1525746113, 2016.

Xin, J., Gong, C., Wang, S., and Wang, Y.: Aerosol direct radiative forcing in desert and semi-desert regions of northwestern China, Atmos. Res., 171, 56-65, https://doi.org/10.1016/j.atmosres.2015.12.004, 2016.

Xu, T., Song, Y., Liu, M., Cai, X., Zhang, H., Guo, J., and Zhu, T.: Temperature inversions in severe polluted days derived from radiosonde data in North China from 2011 to 2016, Sci. Total Environ., 647, 1011-1020, https://doi.org/10.1016/j.scitotenv.2018.08.088, 2019.

Yu, H., Liu, S., and Dickinson, R.: Radiative effects of aerosols on the evolution of the atmospheric boundary layer, J. Geophys. Res., 107(D12), 1, 4142–14, https://doi.org/10.1029/2001JD000754, 2002.

Yang, Y., Liao, H., and Lou, S.: Increase in winter haze over eastern China in recent decades: Roles of variations in meteorological parameters and anthropogenic emissions, J. Geophys. Res.: Atmos., 121, 13050-13065, https://doi.org/10.1002/2016jd025136, 2016.

Zhang, Q., Ma, Q., Zhao, B., Liu, X., Wang, Y., Jia, B., and Zhang, X.: Winter haze over North China Plain from 2009 to 2016: Influence of emission and meteorology, Environ. Pollut., 242, 1308-1318, https://doi.org/10.1016/j.envpol.2018.08.019, 2018.

Zhang, R., Khalizov, A. F., Pagels, J., Zhang, D., Xue, H., and McMurry, P. H.:

Variability in morphology, hygroscopicity, and optical properties of soot aerosols during atmospheric processing, Proc. Natl. Acad. Sci. U. S. A., 105, 10291-10296, https://doi.org/10.1073/pnas.0804860105, 2008.

Zhang, Z., Zhang, X., Zhang, Y., Wang, Y., Zhou, H., Shen, X., Che, H., Sun, J., and Zhang, L.: Characteristics of chemical composition and role of meteorological factors during heavy aerosol pollution episodes in northern Beijing area in autumn and winter of 2015, Tellus B, 69, https://doi.org/10.1080/16000889.2017.1347484, 2017.

Zhao, D., Xin, J., Gong, C., Quan, J., Liu, G., Zhao, W., Wang, Y., Liu, Z., and Song, T.: The formation mechanism of air pollution episodes in Beijing city: Insights into the measured feedback between aerosol radiative forcing and the atmospheric boundary layer stability, Sci. Total Environ., 692, 371-381, https://doi.org/10.1016/j.scitotenv.2019.07.255, 2019.

Zheng, C., Zhao, C., Zhu, Y., Wang, Y., Shi, X., Wu, X., Chen, T., Wu, F., and Qiu, Y.: Analysis of influential factors for the relationship between $PM_{2.5}$ and AOD in Beijing, Atmos. Chem. Phys., 17, 13473-13489, https://doi.org/10.5194/acp-17-13473-2017, 2017.

Zheng, G. J., Duan, F. K., Su, H., Ma, Y. L., Cheng, Y., Zheng, B., Zhang, Q., Huang, T., Kimoto, T., Chang, D., Poeschl, U., Cheng, Y. F., and He, K. B.: Exploring the severe winter haze in Beijing: the impact of synoptic weather, regional transport and heterogeneous reactions, Atmos. Chem. Phys., 15, 2969-2983, https://doi.org/10.5194/acp-15-2969-2015, 2015.

Zhong, J., Zhang, X., Wang, Y., Sun, J., Zhang, Y., Wang, J., Tan, K., Shen, X., Che, H., Zhang, L., Zhang, Z., Qi, X., Zhao, H., Ren, S., and Li, Y.: Relative Contributions of Boundary-Layer Meteorological Factors to the Explosive Growth of $PM_{2.5}$ during the Red-Alert Heavy Pollution Episodes in Beijing in December 2016, J. Meteorol. Res., 31, 809-819, https://doi.org/10.1007/s13351-017-7088-0, 2017.

Zhong, J., Zhang, X., Wang, Y., Liu, C., and Dong, Y.: Heavy aerosol pollution episodes in winter Beijing enhanced by radiative cooling effects of aerosols, Atmos. Res.,

209, 59-64, https://doi.org/10.1016/j.atmosres.2018.03.011, 2018a.

Zhong, J., Zhang, X., Dong, Y., Wang, Y., Liu, C., Wang, J., Zhang, Y., and Che, H.: Feedback effects of boundary-layer meteorological factors on cumulative explosive growth of PM2.5 during winter heavy pollution episodes in Beijing from 2013 to 2016, Atmos. Chem. Phys., 18, 247–258, https://doi.org/10.5194/acp-18-247-2018, 2018b.

Zhong, J., Zhang, X., Wang, Y., Wang, J., Shen, X., Zhang, H., Wang, T., Xie, Z., Liu, C., Zhang, H., Zhao, T., Sun, J., Fan, S., Gao, Z., Li, Y., and Wang, L.: The two-way feedback mechanism between unfavorable meteorological conditions and cumulative aerosol pollution in various haze regions of China, Atmos. Chem. Phys., 19, 3287–3306, https://doi.org/10.5194/acp-19-3287-2019, 2019.

Zhu, X., Tang, G., Lv, F., Hu, B., Cheng, M., Muenkel, C., Schafer, K., Xin, J., An, X., Wang, G., Li, X., and Wang, Y.: The spatial representativeness of mixing layer height observations in the North China Plain, Atmos. Res., 209, 204-211, https://doi.org/10.1016/j.atmosres.2018.03.019, 2018.